Conformational flexibility within the small domain of human serine racemase

Chloe R. Koulouris, Benjamin D. Bax, John R. Atack and S. Mark Roe

IUCr Journals
CRYSTALLOGRAPHY JOURNALS ONLINE

Conformational flexibility within the small domain of human serine racemase

Chloe R. Koulouris,[a]* Benjamin D. Bax,[b]* John R. Atack[b]* and S. Mark Roe[c]

[a]Sussex Drug Discovery Centre, University of Sussex, Falmer, Brighton BN1 9QG, England, [b]Medicines Discovery Institute, School of Biosciences, University of Cardiff, Park Place, Cardiff CF10 3AT, Wales, and [c]Department of Biochemistry and Biomedicine, School of Life Sciences, University of Sussex, Falmer, Brighton BN1 9QJ, England. *Correspondence e-mail: c.koulouris@sussex.ac.uk, baxb@cardiff.ac.uk, atackj@cardiff.ac.uk

Serine racemase (SR) is a pyridoxal 5′-phosphate (PLP)-containing enzyme that converts L-serine to D-serine, an endogenous co-agonist for the N-methyl-D-aspartate receptor (NMDAR) subtype of glutamate ion channels. SR regulates D-serine levels by the reversible racemization of L-serine to D-serine, as well as the catabolism of serine by α,β-elimination to produce pyruvate. The modulation of SR activity is therefore an attractive therapeutic approach to disorders associated with abnormal glutamatergic signalling since it allows an indirect modulation of NMDAR function. In the present study, a 1.89 Å resolution crystal structure of the human SR holoenzyme (including the PLP cofactor) with four subunits in the asymmetric unit is described. Comparison of this new structure with the crystal structure of human SR with malonate (PDB entry 3l6b) shows an interdomain cleft that is open in the holo structure but which disappears when the inhibitor malonate binds and is enclosed. This is owing to a shift of the small domain (residues 78–155) in human SR similar to that previously described for the rat enzyme. This domain movement is accompanied by changes within the twist of the central four-stranded β-sheet of the small domain, including changes in the φ–ψ angles of all three residues in the C-terminal β-strand (residues 149–151). In the malonate-bound structure, Ser84 (a catalytic residue) points its side chain at the malonate and is preceded by a six-residue β-strand (residues 78–83), but in the holoenzyme the β-strand is only four residues (78–81) and His82 has φ–ψ values in the α-helical region of the Ramachandran plot. These data therefore represent a crystallographic platform that enables the structure-guided design of small-molecule modulators for this important but to date undrugged target.

1. Introduction

N-Methyl-D-aspartate receptors (NMDARs) are a subtype of ionotropic glutamate receptors that are highly expressed in the central nervous system (CNS) and are involved in the excitatory synaptic transmission and synaptic plasticity that form the basis of many critical CNS functions (Traynelis *et al.*, 2010). Glutamatergic and more specifically NMDAR dysfunction has been implicated in various CNS disorders, including Alzheimer's disease (Zádori *et al.*, 2014; Balu *et al.*, 2019), amyotrophic lateral sclerosis (ALS; Paul & de Beller-oche, 2014), neuropathic pain (Petrenko *et al.*, 2003), schizophrenia (Howes *et al.*, 2015) and major depressive disorder (Niciu *et al.*, 2014). Most nonselective, direct NMDAR antagonists (such as ketamine) that have shown efficacy at relieving symptoms of neuropathic pain (Zhou *et al.*, 2011) and treatment-resistant depression (TRD; Daly *et al.*, 2019; Vasilescu *et al.*, 2017) have undesirable side effects that restrict their clinical utility (Pomarol-Clotet *et al.*, 2006; Niesters *et al.*,

electronic reprint
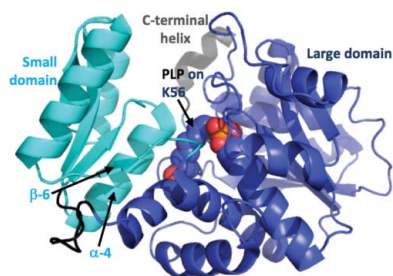
2014; Schatzberg, 2019). Hence, indirect or subtype-specific modulators of NMDAR function offer the potential to have reduced side effects relative to nonselective antagonists. One approach is to target the NMDAR co-agonist D-serine, which is required for the activation of NMDARs via binding to the glycine modulatory site, so-called because glycine is an alternative endogenous co-agonist (Kleckner & Dingledine, 1988). The neuroanatomical distribution suggests that D-serine is primarily localized to the forebrain, with a distribution that mirrors that of the GluN2A- and GluN2B-containing subtypes of NMDAR, while glycine is predominantly located in the hindbrain and brainstem, indicating a potentially selective avenue for modulating glutamate neurotransmission in the CNS (Papouin et al., 2012). The critical role of D-serine has been described in neuropsychiatric conditions including schizophrenia (Tsai et al., 1998; Hashimoto et al., 2003; Labrie et al., 2012), depression (Malkesman et al., 2012; Otte et al., 2013) and Alzheimer's disease (Hashimoto et al., 2004; Wu et al., 2004; Madeira et al., 2015). The recent approval of esketamine, an enantiomer of racemic ketamine, as a nasal spray for treatment-resistant depression (Daly et al., 2019; Schatzberg, 2019; Swainson et al., 2019; Fedgchin et al., 2019) demonstrates the therapeutic value of targeting NMDARs.

Serine racemase (SR) is a pyridoxal 5′-phosphate (PLP)-containing enzyme that converts L-serine to D-serine (Wolosker et al., 1999); therefore, inhibitors of SR that reduce the production of D-serine are hypothesized to have therapeutic benefits in disorders associated with NMDAR hyperfunction (Coyle & Balu, 2018). Almost all endogenous D-serine is produced by SR, as demonstrated by the observation that SR-knockout mice have an 80–90% reduction in D-serine levels (Balu et al., 2013). Several groups have tried to identify new SR inhibitors that are potent, selective and structurally distinct from the many well described amino-acid analogues, but overall there has been relatively little progress (Jirásková-Vaníčková et al., 2011; Beato et al., 2015; Vorlová et al., 2015; Watanabe et al., 2016; Mori et al., 2017). One of the more promising approaches identified a series of dipeptide-like inhibitors with a clear structural motif and slow-binding kinetics (Dixon et al., 2006), which later provided the query molecule for an in silico screen (Mori et al., 2014). The resulting amide inhibitors and halogen-substituted derivatives showed improved inhibitory activity (compared with classical SR inhibitors), binding affinity and ligand efficiency, but limited potency, with reported IC_{50} values of 0.28, 0.27 and 0.14 mM for the best compounds (Mori et al., 2017). Overall, there are a negligible number of drug-like SR inhibitors and none that have been confirmed by crystallography.

X-ray crystal structures of mammalian SR were first published for the rat holoenzyme (1.8 Å resolution) and the rat and human malonate (an orthosteric inhibitor)-bound complexes (1.9 and 1.5 Å resolution), and more recently for the wild-type human holoenzyme (1.8 Å resolution) (Takahara et al., 2018; Smith et al., 2010). SR is organized as a dimer, with each monomer comprised of a large domain containing the essential PLP cofactor covalently bound to Lys56 and a small domain that undergoes a ligand-induced reorientation

upon binding at the domain interface (Smith et al., 2010). The organization of the domain boundaries is described as follows for the human SR–malonate complex (PDB entry 3l6b; Smith et al., 2010): the small domain (residues 55–151) contains a central four-stranded β-sheet (residues 149–151, 78–83, 101–108 and 124–128) and four α-helices (residues 55–66, 85–98, 111–121 and 131–147), and the large domain (residues 1–68 and 157–340) contains a seven-stranded twisted β-sheet surrounded by ten α-helices.

PLP-dependent enzymes can be categorized as fold types I–IV, according to the similarity of their secondary structure (Jansonius, 1998). SR belongs to the fold type II family, along with its closest homologue serine dehydratase (SDH). SDH is a mammalian enzyme that catalyses the dehydration of L-serine to pyruvate and ammonia, and shares 23% sequence identity with SR. Proteins in this group have two domains and each contains a β-sheet core surrounded by α-helices. Accordingly, the small domain of SDH consists of a central four-stranded β-sheet surrounded by four α-helices (Yamada et al., 2003; Sun et al., 2005), and corresponds to residues 55–151 of SR. In the original crystal structure paper, Smith and coworkers defined the small domain as residues 78–155, and did not include helix 3 (55–66) in the small domain because it precedes a mobile hinge region (residues 69–77) and is not involved in the rearrangement of the small domain (Smith et al., 2010). Further, their definition of a flexible loop region connecting both domains comprised of residues 68–77 and 145–149 (Smith et al., 2010) is somewhat problematic as residues 145–149 are defined as being within the small domain and are before the final β-strand of the central β-sheet.

In the present study, we have determined the structure of the holo form of human SR and used this in structural comparisons with the previously published human malonate-bound complex. We have used the more soluble Cys2Asp, Cys6Asp mutant (Smith et al., 2010; Section 2) as this construct improves the solubility during the purification process, while producing no significant structural changes at the N-terminus when compared with wild-type protein (PDB entry 5x2l; Takahara et al., 2018). Moreover, we have sought to clarify the ambiguity regarding the domain-boundary definitions of SR, particularly in the context of ligand-induced small domain rearrangement. A more developed understanding of the conformational changes that occur upon malonate binding may further inform and enable strategies, such as structure-guided drug design, for the development of novel inhibitors of SR with more drug-like properties.

2. Materials and methods

2.1. Macromolecule production

The pET-24a vector containing a C-terminal polyhistidine (His_6) tag and two cysteine-to-aspartate point mutations (Cys2Asp, Cys6Asp) to improve solubility during the purification process (Smith et al., 2010) and improve the overall yield (unpublished observations) was chemically transformed into Escherichia coli BL21 CodonPlus(DE3)-RIL cells, and

Table 1
Macromolecule-production information.

DNA source	pET-24a vector containing the human SR gene with two point mutations (Cys2Asp, Cys6Asp) and a C-terminal His$_6$ tag kindly donated by Evotec for the purposes of this research
Cloning vector	pUC57
Expression vector	pET-24a
Expression host	*E. coli* BL21 CodonPlus(DE3)-RIL
Complete amino-acid sequence of the construct produced	MD**A**QY**D**ISFADVEKAHINIRDSIHLTPVLT SSILNQLTGRNLFFKCELFQKTGSFKIR GALNAVRSLVPDALERKPKAVVTHSSGN HGQALTYAAKLEGIPAYIVVPQTAPDCK KLAIQAYGASIVYCEPSDESRENVAKRV TEETEGIMVHPNQEPAVIAGQGTIALEV LNQVPLVDALVVPVGGGGMLAGIAITVK ALKPSVKVYAAEPSNADDCYQSKLKGKL MPNLYPPETIADGVKSSIGLNTWPIIRD LVDDIFTVTEDEIKCATQLVWERMKLLI EPTAGVGVAAVLSQHFQTVSPEVKNICI VLSGGNVDLTSSITWVKQAERPASYQSV SVHHHHHH

Table 2
Crystallization.

Method	Sitting-drop vapour diffusion
Plate type	MRC Maxi 48-well
Temperature (K)	293
Protein concentration (mg ml^{-1})	6.5
Buffer composition of protein solution	20 m*M* Tris–HCl pH 8.0, 100 m*M* NaCl, 10% glycerol, 1 m*M* MgCl$_2$, 0.5 m*M* ATP, 50 µ*M* PLP, 5 m*M* DTT
Composition of reservoir solution	100 m*M* bis-Tris pH 6.5, 15% PEG 3350, 250 m*M* MgCl$_2$
Volume and ratio of drop	2 µl, 1:1
Volume of reservoir (µl)	100

Table 3
Data collection and processing.

Values in parentheses are for the outer shell.

Diffraction source	I03, Diamond Light Source
Wavelength (Å)	0.97625
Temperature (K)	100
Detector	PILATUS3 6M, Dectris
Crystal-to-detector distance (mm)	342.34
Rotation range per image (°)	0.1
Total rotation range (°)	180
Exposure time per image (s)	0.1
Space group	$P2_1$
a, b, c (Å)	48.20, 155.74, 85.58
α, β, γ (°)	90, 98.48, 90
Mosaicity (°)	0.184
Resolution range (Å)	42.73–1.89 (1.92–1.89)
Total No. of reflections	331938 (16869)
No. of unique reflections	98693 (4996)
Completeness (%)	99.2 (99.7)
Multiplicity	3.4 (3.4)
$\langle I/\sigma(I) \rangle$	10.5 (1.5)
R_{merge}	0.061 (0.947)
$R_{r.i.m.}$	0.071 (1.086)
$CC_{1/2}$	0.997 (0.543)
Overall B factor from Wilson plot (Å^2)	36.3

plated onto LB agar plates (50 µg ml^{-1} kanamycin and 35 µg ml^{-1} chloramphenicol) for overnight incubation at 37°C. Pre-cultures grown overnight in LB from a single colony at 37°C were used to inoculate 8 × 1 l LB medium supplemented with 50 µg ml^{-1} kanamycin, 34 µg ml^{-1} chloramphenicol and 0.01% pyridoxine (the enzyme contains PLP as a cofactor). The cells were grown at 37°C to an optical density at 600 nm (OD$_{600}$) of 0.6, at which point gene expression was induced with 0.5 m*M* isopropyl β-D-1-thiogalactopyranoside (IPTG) and cell growth was continued for a further 16–18 h at 25°C. The cells were harvested by centrifugation at 6500*g* for 20 min at 4°C and stored at −80°C.

The cell pellet was solubilized and lysed by sonication while on ice and the lysate was then clarified at 25 000*g* for 60 min at 4°C. The supernatant was loaded onto a TALON column for initial purification by immobilized-metal affinity chromatography via interaction of the SR His tag with the nickel-containing beads of the TALON resin. The protein-containing fractions (as determined by SDS–PAGE) were loaded onto a Superdex 200 (26/60) column equilibrated with buffer consisting of 20 m*M* Tris pH 8.0, 100 m*M* NaCl, 5 m*M* DTT, 50 µ*M* PLP, 1 m*M* MgCl$_2$, 10% glycerol. The SR-containing fractions (as determined by SDS–PAGE) were pooled and concentrated to 15 mg ml^{-1} before being flash-frozen in liquid nitrogen and stored at −80°C. The protein concentration was determined by UV spectrophotometry at 280 nm using a molar extinction coefficient of 29 910 *M*$^{-1}$ cm^{-1} and a molecular weight of 37.4 kDa. The protein yield was approximately 3 mg per litre of culture and the purified protein had a purity of >95%. Macromolecule-production information is summarized in Table 1.

2.2. Crystallization

Human holo SR was crystallized by the sitting-drop vapour-diffusion method. A reservoir solution consisting of 15% PEG 3350, 100 m*M* bis-Tris pH 6.5, 250 m*M* MgCl$_2$ was mixed with the protein solution (6.5 mg ml^{-1} SR and 5 m*M* DTT) in a 1:1 ratio and equilibrated at 20°C. Crystals appeared within 48 h and grew to full size (∼50 µm) within seven days. The crystal used for the diffraction experiment was cryoprotected by sequential soaking in reservoir solution supplemented with 10%, 20% and 30% glycerol prior to data collection. Crystallization information is summarized in Table 2.

2.3. Data collection and processing

An X-ray data set was collected from a single cryocooled crystal on beamline I03 at the Diamond Light Source synchrotron (Table 3).

2.4. Structure solution and refinement

The structure was solved by molecular replacement using the crystal structure of the rat SR holoenzyme (Smith *et al.*, 2010; the rat holoenzyme was used because structure solution occurred prior to the deposition of PDB entry 5x2l) and was refined with *REFMAC*5 (Murshudov *et al.*, 2011) and *phenix.refine* (Adams *et al.*, 2010) with iterative cycles of model building in *Coot* (Emsley *et al.*, 2010). The final structure had reasonable geometry and *R* factors (Table 4) and the

four subunits in the asymmetric unit contained residues *A*4–*A*325, *B*4–*B*326, *C*3–*C*325 and *D*4–*D*325.

Towards the end of the refinement, difference maps clearly showed electron density for a second position for the β-strands in the central β-sheet of the small domain in the *C* subunit (the small domain of human SR is defined as residues 78–155). The small domain from the *C* subunit (residues *C*74–*C*152) was rigid-body fitted into the difference map in *Coot*, and the new position (and the original position) were refined with occupancies in steps of 0.1 (0.1/0.9, 0.2/0.8 *etc.*). Lower *R* factors (and R_{free}) suggested that the occupancy of the alternate 'new' position was approximately 0.3 (and that of the original position was 0.7). There is some variability in the position of the small domain relative to the large domain when all four subunits are compared (Supplementary Fig. S1).

Across the four chains in the asymmetric unit (*A*, *B*, *C* and *D*), the overall ordering of the residues was reasonable, with exceptions at the N-terminus (residues 1–3) and C-terminus (residues 326–340). The small domains (residues 78–151) appear to be more mobile, with higher temperature factors (57.1, 100.4, 76.9 and 66.4 Å^2 for the small domains from chains *A*, *B*, *C* and *D*, respectively, compared with 34.9, 58.4, 53.7 and 38.6 Å^2 for the corresponding large domains). The flexible loop region (residues 66–77) is complete and well defined only in chain *A*, which is likely to be an effect of crystal packing. The Ramachandran plot reveals good stereochemistry and negligible steric hindrances between atoms of the polypeptide backbone, with 99.6% of residue angles falling within the allowed regions and 96% within favoured regions (Table 4).

2.5. Structure analysis

Secondary structures were calculated with the *PDBSUM* server (Laskowski *et al.*, 2018), including HERA plots of secondary structure (Hutchinson & Thornton, 1990). The secondary structure of the *A* subunit from our 1.89 Å resolution holoenzyme structure (PDB entry 6slh), as calculated with the *PDBSUM* server, was manually checked against electron density in *Coot* (Emsley *et al.*, 2010). This secondary structure was compared with that defined in the PDB headers of the 1.5 Å resolution human SR structure in complex with malonate (PDB entry 3l6b; Smith *et al.*, 2010) and the 1.81 Å resolution crystal structure of wild-type SR (PDB entry 5x2l; Takahara *et al.*, 2018). The *PDBSUM* server definitions of secondary structure for PDB entries 3l6b and 5x2l were also checked (see Supplementary Table S1 for definitions and comparisons of secondary-structure elements). This analysis defined the positions of the ten β-strands (β1–β10), 12 α-helices (α1–α12) and five 3$_{10}$-helices in our structure (Supplementary Table S1). We note that although serine dehydratase belongs to the same overall fold type as SR, it lacks the N-terminal helix of SR and its C-terminal helix is an α-helix rather than the 3$_{10}$-helix often seen in SR structures (Supplementary Table S1).

Secondary-structure definitions were inserted into the PDB headers before drawing structures with *PyMOL* (v.1.5.0.4;

Table 4
Structure refinement.

Values in parentheses are for the outer shell.

Resolution range (Å)	40.874–1.890 (1.939–1.890)
σ Cutoff	None
No. of reflections, working set	93727 (6987)
No. of reflections, test set	4925 (351)
Final R_{cryst}	0.172 (0.294)
Final R_{free}	0.216 (0.302)
Cruickshank DPI	0.246†
No. of non-H atoms	
Protein	8309
Ion	6
Ligand	124
Water	531
R.m.s. deviations	
Bond lengths (Å)	0.011
Angles (°)	1.859
Average *B* factors (Å^2)	
Protein	53.0 [46.5 for large domain]‡
Ramachandran plot	
Most favoured (%)	96
Allowed (%)	3.6
Outliers (%)	0.4

† Calculated by the *Online_DPI* server (Kumar *et al.*, 2015). ‡ The small domain had higher *B* factors than the large domain.

Schrödinger). The Kleywegt (Ramachandran) plots (Kleywegt & Jones, 1996) were drawn in *Coot* (Emsley *et al.*, 2010). φ–ψ angles were calculated with the *CCP*4 program *ANGLES* (Winn *et al.*, 2011) and are presented in Supplementary Table S2.

The small domain is defined as residues 78–155 and the large domain as residues 1–68 and 156–316. R.m.s. fits were calculated with *LSQKAB* (Winn *et al.*, 2011) for all C$^\alpha$ atoms or subsets of C$^\alpha$ atoms between the *A* subunit of our new 1.89 Å resolution human SR structure and the previously determined structure in complex with malonate (PDB entry 3l6b) and holo structure in a different cell (PDB entry 5x2l) (see Supplementary Table S3). In the two holo structures the large and small domains are in roughly the same position, whereas in the complex with malonate the small domain is in a different position with respect to the large domain.

3. Results and discussion

3.1. Human SR holoenzyme structure

The crystal structure of the human SR holoenzyme was determined to a resolution of 1.89 Å in space group $P2_1$ and reveals the large domain (residues 1–68 and 156–316) and the small domain (residues 78–155) (Fig. 1*a*) connected by a flexible loop region (residues 66–77) at the N-terminus of the small domain. The PLP catalytic cofactor is covalently linked to Lys56 via a Schiff-base linkage between the side chain of the lysine and the carbonyl C atom of PLP. The C-terminal β-strand (residues 149–151) of the small domain can change its φ–ψ angles (twist) to allow domain movement. Our definition of the small domain (residues 78–155) agrees with that taken from Smith *et al.* (2010), whereas our definition of the large domain (residues 1–68 and 156–316) differs from theirs

(residues 1–68 and 157–340) in that we do not include the C-terminal 3_{10}-helix (residues 319–325) and subsequent disordered residues. The recently published holoenzyme crystal structure of wild-type human SR (PDB entry 5x2l; Takahara *et al.*, 2018), which did not have the two N-terminal mutations Cys2Asp and CysC6Asp (see Section 2.1), has a very similar structure at the N-terminus. However, PDB entry 5x2l is shorter at the C-terminus (the last residue is 317) and does not have the C-terminal 3_{10}-helix (see Supplementary Table S1 for a description of the secondary-structural elements used in this paper). Regardless of some local structural differences, the overall structures of PDB entries 6slh and 5x2l superpose well, with a C^{α} r.m.s.d. of 0.55 Å.

The C-terminal helix (residues 319–325) of PDB entry 6slh is located at the dimer interface and appears to have some degree of flexibility, which may reflect a role in dimerization and stabilization of the protein complex. Indeed, the C-terminal 3_{10}-helices are in close proximity to each other in chains A/C and B/D, and the interfaces of each pair of helices are lined with hydrophobic residues (Leu319, Thr320, Ile323 and Val326) that indicate the presence of dimerizing hydrophobic interactions. It has been suggested that the activity of SR may be regulated by interactions of its C-terminal residues with a PDZ domain from GRIP (Baumgart *et al.*, 2007).

In accordance with the characteristics of fold type II PLP-dependent enzymes, our SR holoenzyme structure reveals a small domain with a central β-sheet consisting of four parallel β-strands (residues 78–81, 101–108, 124–128 and 149–151) flanked by two α-helices on one side (residues 85–98 and 111–121) and one α-helix (residues 131–146) on the other side. The large domain has a six-stranded β-sheet core surrounded by α-helices, and this domain arrangement is conserved between the malonate complex (PDB entry 3l6b) and our holoenzyme structure. A magnesium ion resides in the divalent cation-binding site, where it is coordinated by three buried waters, two acidic side chains (Glu210 and Asp216) and the
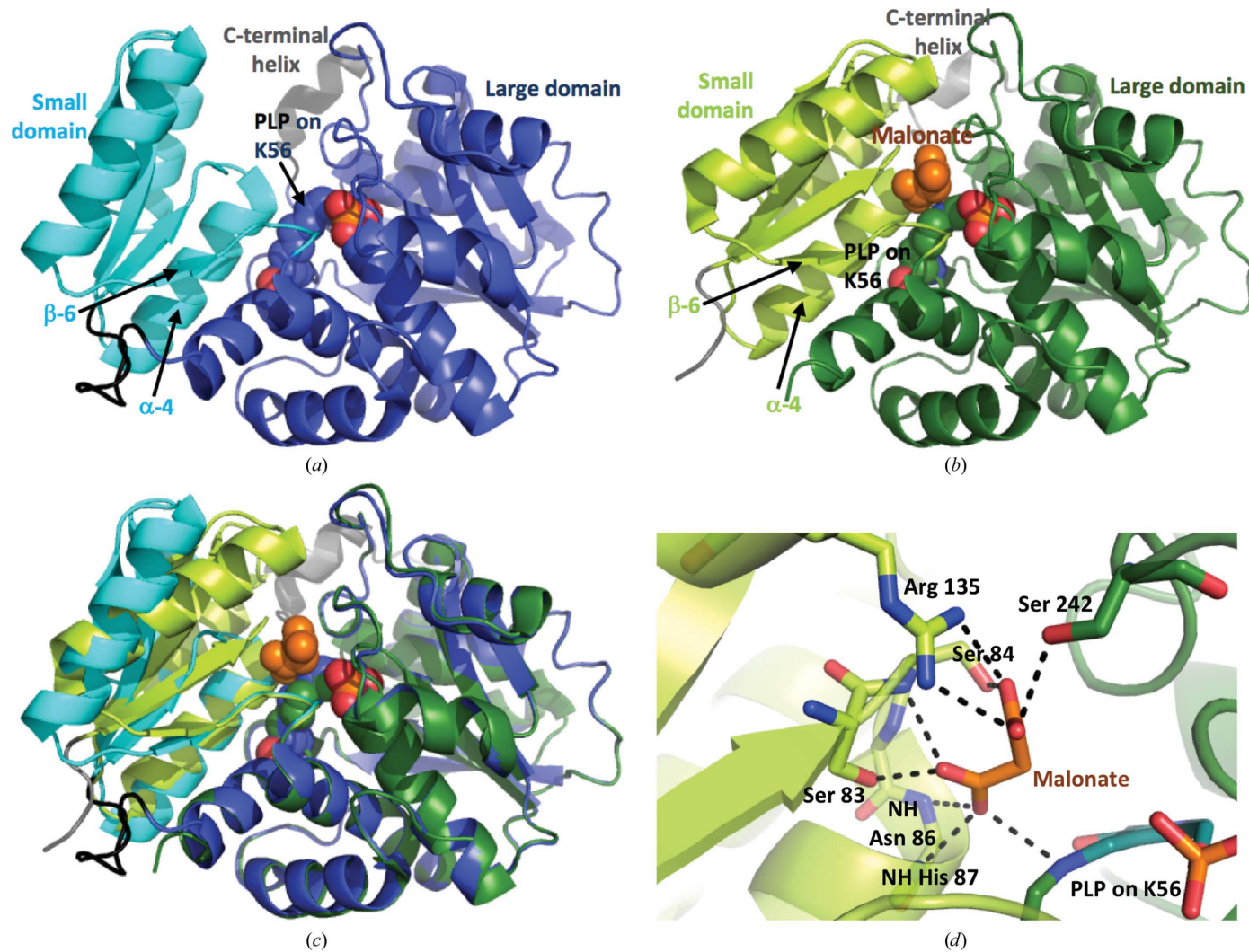

Figure 1
Overall comparison of the new holo human SR structure with that of a malonate complex (PDB entry 3l6b). (*a*) One human SR monomer from the 1.89 Å resolution holo structure. Each subunit has a large domain (dark blue) and a small domain (cyan). The C-terminal 3_{10}-helix is shown in grey. The essential cofactor PLP covalently bound to Lys56 is shown in sphere representation. (*b*) The human SR subunit from the structure with malonate (orange spheres) is shown with the small domain in pale green and the large domain in dark green. (*c*) Superposition of the large domains of the structures in (*a*) and (*b*). Note how most, but not all, of the small domain is shifted. (*d*) Close-up view of the malonate-binding site in a similar orientation to (*b*).
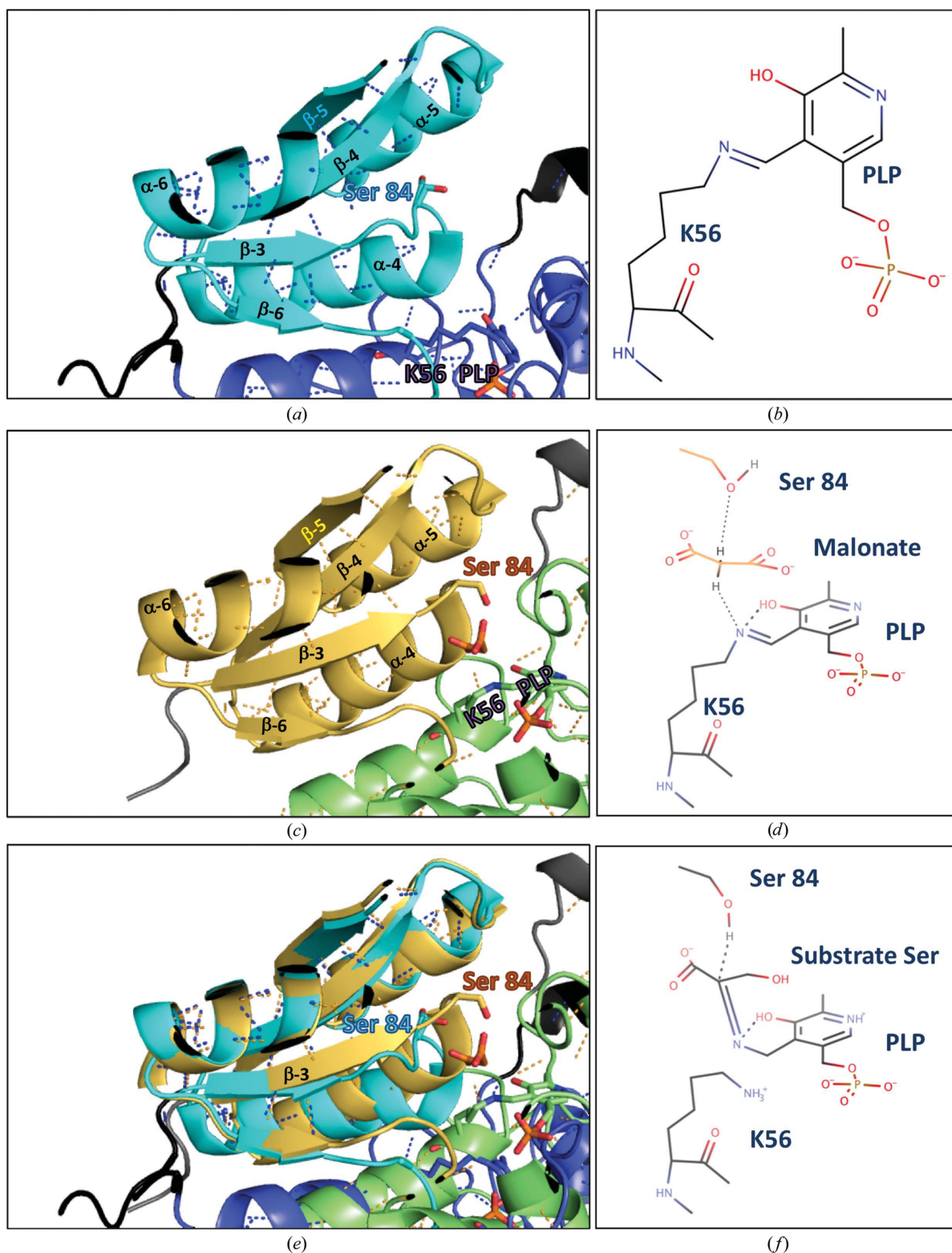
Figure 2
Superposition of the small domains of human SR structures. (a) The small domain (cyan) from the 1.89 Å resolution human SR structure contains secondary-structural elements labelled β-3, α-4, β-4, α-5, β-5, α-6 and β-6. Also shown are main-chain hydrogen bonds (dark blue), the C-terminal 3_{10}-helix (dark grey) and the 67–77 loop (dark grey). The Ser84 side chain (modelled in two rotamers) is shown in stick representation. (b) PLP attached to Lys56 drawn with *MarvinSketch* using the most likely tautomer at pH 7.0 (there are 14 possible tautomers between pH 4 and 10). (c) The human SR subunit from a structure with malonate (PDB entry 3l6b) is shown with the small domain in yellow and the large domain in light green. The Ser84 side chain is shown in stick representation pointing at malonate (orange sticks). Main-chain hydrogen bonds are shown in orange. (d) Chemical representation of the structure in (c). Dotted lines are possible hydrogen bonds (length of <3.3 Å). (e) Superposition of the small domains of the structures in (a) and (c). Note how most of the small domain is reasonably well superposed, but Ser84 and the α-4 helix are in different positions. (f) Ser84 is believed to protonate the substrate serine to convert it to D-serine.

main-chain carbonyl of Ala214, thus helping to stabilize protein folding and increase maximal activity (De Miranda *et al.*, 2002; Bruno *et al.*, 2017). While the domain structure and most secondary-structural elements are conserved between SR and SDH, SDH lacks the N-terminal α-helix and has a C-terminal α-helix, rather than the C-terminal 3_{10}-helix seen in some human SR structures (Supplementary Table S1).

3.2. The small domain is in an 'open' position in the holo structure

Comparing the structures of holo (Fig. 1*a*) and malonate-bound (Fig. 1*b*) human SR using a superposition based on residues from the large domains showed a relative large shift of most of the small domain (Fig. 1*c*). There is a striking difference between the accessibility of the active site in the two structures. In the malonate-bound form (Figs. 1*b* and 1*d*) the small domain is positioned tight against the large domain to form a 'closed' structure in which the catalytic site is inaccessible to solvent; notably, helices α5 and α6 shift towards PLP in the large domain by distances of about 5.5 and 8 Å, respectively. In the holoenzyme structure, the high degree of mobility of the small domain and flexible loop region is shown by the distance between the two domains, creating an 'open' position large enough to allow the binding of an amino acid, small molecule or compound.

When malonate is bound in the active site (Fig. 1*d*) it forms hydrogen bonds between its two carboxylic acid groups and the surrounding residues: the hydroxyl groups of Ser84 and Ser242, the amino groups of Ser84 and His87 and the side chain of Arg135 (Fig. 1*d*). The dual carboxylic acid nature of malonate allows it to induce a conformational shift linking the large domain and Ser84, the key catalytic site residue located in the small domain. In a proposed mechanism of L-serine isomerization, PLP and L-serine are linked by a protonated Schiff base, and PLP then deprotonates L-serine to form a planar intermediate. Ser84 is moved into position via a ligand-induced shift on the opposite side of the PLP ring plane to donate a proton from its hydroxyl group and thus invert the stereochemistry of L-serine to D-serine (Yoshimura, 2008; Goto *et al.*, 2009).

The commonly accepted reaction mechanism of mammalian SR is based on data from bacterial enzymes and comparisons between human, rat and yeast orthologues (Goto *et al.*, 2009; Smith *et al.*, 2010). The major structural change between human holo and malonate-bound SR described here further supports the existence of an analogous mechanism for L-serine isomerization in the human enzyme. Moreover, the 'open' conformation of the human SR holoenzyme suggests that the active site and key catalytic residues are accessible to small molecules and compounds, and indicates that SR is structurally enabled for drug-discovery efforts and *in silico* screening.

3.3. Conformational flexibility with the small domain of human SR

A superposition of holo (Fig. 2*a*) and malonate-bound (Fig. 2*c*) human SR based on residues from the small domains

(residues 78–155) show that not all residues within the small domain of human SR 'move' with the small domain. Notably, the α4 helix (residues 85–99) and residues at the C-terminal end of the domain (residues 153–155) do not move with the rest of the small domain but seem to remain relatively static with regard to the large domain (Fig. 1*c*). Thus, we have defined a small mobile subdomain (residues 78–81 and 101–148) which appears to be linked to the rest of SR by four


(a)

(b)
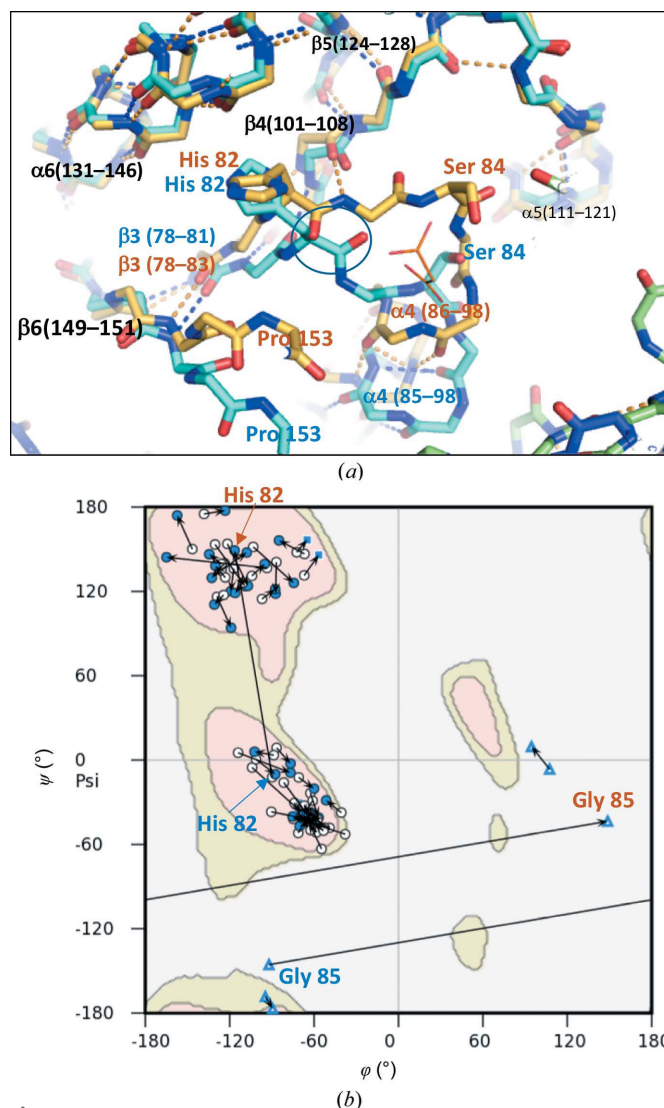
Figure 3
Conformational flexibility within the small domain of the human SR structure. (*a*) Main-chain atoms from the small domain of human SR, close to Ser84, are shown with N atoms in blue, O atoms in red, C atoms in cyan for the holo structure and yellow for the malonate-bound structure (PDB entry 3l6b), and main-chain hydrogen bonds as dashed blue or orange lines. The small domains are superposed as in Fig 2(*c*). The loop connecting the C-terminus of β3 to the N-terminus of α4 has a different conformation, and the α4 helix from the small domain is not well superposed. (For clarity, only the side chains of His82 and Ser84 are shown. Note how the carbonyl O atoms of His82, which are ringed, are pointing in different directions.) (*b*) A Kleywegt plot comparing the small domain of holo SR (subunit *D*) with that in a malonate-bound structure (PDB entry 3l6b). The plot shows arrows between the same residue in the two structures. Residues that have large differences in φ–ψ are labelled (blue for holo φ–ψ, orange for malonate φ–ψ). The φ–ψ angles in this region are presented in Supplementary Table S2.

flexible hinge regions (residues 68–77, 82–85, 99–101 and 149–151), which were defined based on further analysis of the small domain (Fig. 3). Our data show that the loop that contains Ser84 undergoes a dramatic change in conformation between the holo and ligand-bound structures (Fig. 3a), with two residues, His82 and Gly85, having very different conformations (Fig. 3b). A comparison of φ–ψ angles (Supplementary Table S2) demonstrates that not only are there dramatic changes in the φ–ψ angles of His82 and Gly85, but that there is a consistent change in the φ–ψ angles of the three residues in the final β-strand of the small domain (residues 149–151; Supplementary Table S2). This β-strand (residues 149–151), acting as a flexible hinge region, is relatively well superposed whether the superposition is based on the large domain (Fig. 1c) or the small domain (Fig. 2c). Furthermore, a significant change in the conformation of residues 82–85 (Fig. 3) indicates that this is an additional loop region, which may function to prevent any catalysis occurring until the substrate is fully captured in an enclosed active site.

4. Discussion

When large structural movements take place within a single globular structural domain (for example between the GDP- and GTP-bound forms of the small GTPase ARF; Goldberg, 1998), subdivision of the structural domain into subdomains that 'move' relative to each other in different states of the protein may become relevant. We have analysed secondary- and tertiary-structure elements in our human holoenzyme SR structure and in a malonate complex of SR (PDB entry 3l6b) to define 'moving' and 'relatively static' subdomains within the small domain of human serine racemase, and we show that only part of the small domain moves upon the binding of malonate. While the crystal structure presented here appears to have high global structural homology to previous SR structures (PDB entries 5x2l and 3l6b), our observations regarding the movement of the small domain subdomain and the presence of four flexible hinge regions differs from previous assertions in that the ligand binding induced movement of the entire small domain flanked by two loop regions (Smith *et al.*, 2010). Structural knowledge of SR subdomain rearrangement is important for *in silico* drug design, pharmacophore modelling and screening, and provides additional information for determining how conformational changes of the hinge regions and subdomain alter binding in the active site.

Acknowledgements

We are especially grateful to Evotec, particularly Myron Smith, Michael Wood and David Hallett, for their provision of the expression construct and protein-production resources and advice. We also thank Diamond Light Source Ltd (Didcot, UK) for access to synchrotron radiation on beamline I03, the Wellcome Trust for support for X-ray diffraction facilities at the University of Sussex and Raj Gill for useful discussion.

References

Adams, P. D., Afonine, P. V., Bunkóczi, G., Chen, V. B., Davis, I. W., Echols, N., Headd, J. J., Hung, L.-W., Kapral, G. J., Grosse-Kunstleve, R. W., McCoy, A. J., Moriarty, N. W., Oeffner, R., Read, R. J., Richardson, D. C., Richardson, J. S., Terwilliger, T. C. & Zwart, P. H. (2010). *Acta Cryst.* D66, 213–221.

Balu, D. T., Li, Y., Puhl, M. D., Benneyworth, M. A., Basu, A. C., Takagi, S., Bolshakov, V. Y. & Coyle, J. T. (2013). *Proc. Natl Acad. Sci. USA*, **110**, E2400–E2409.

Balu, D. T., Pantazopoulos, H., Huang, C. C. Y., Muszynski, K., Harvey, T. L., Uno, Y., Rorabaugh, J. M., Galloway, C. R., Botz-Zapp, C., Berretta, S., Weinshenker, D. & Coyle, J. T. (2019). *Neurobiol. Dis.* **130**, 104511.

Baumgart, F., Mancheño, J. M. & Rodríguez-Crespo, I. (2007). *FEBS J.* **274**, 4561–4571.

Beato, C., Pecchini, C., Cocconcelli, C., Campanini, B., Marchetti, M., Pieroni, M., Mozzarelli, A. & Costantino, G. (2015). *J. Enzyme Inhib. Med. Chem.* **31**, 645–652.

Bruno, S., Margiotta, M., Marchesani, F., Paredi, G., Orlandi, V., Faggiano, S., Ronda, L., Campanini, B. & Mozzarelli, A. (2017). *Biochim. Biophys. Acta*, **1865**, 381–387.

Coyle, J. T. & Balu, D. T. (2018). *Adv. Pharmacol.* **82**, 35–56.

Daly, E. J., Trivedi, M. H., Janik, A., Li, H., Zhang, Y., Li, X., Lane, R., Lim, P., Duca, A. R., Hough, D., Thase, M. E., Zajecka, J., Winokur, A., Divacka, I., Fagiolini, A., Cubala, W. J., Bitter, I., Blier, P., Shelton, R. C., Molero, P., Manji, H., Drevets, W. C. & Singh, J. B. (2019). *JAMA Psychiatry*, **76**, 893–903.

De Miranda, J., Panizzutti, R., Foltyn, V. N. & Wolosker, H. (2002). *Proc. Natl Acad. Sci. USA*, **99**, 14542–14547.

Dixon, S. M., Li, P., Liu, R., Wolosker, H., Lam, K. S., Kurth, M. J. & Toney, M. D. (2006). *J. Med. Chem.* **49**, 2388–2397.

Emsley, P., Lohkamp, B., Scott, W. G. & Cowtan, K. (2010). *Acta Cryst.* D66, 486–501.

Fedgchin, M., Trivedi, M., Daly, E. J., Melkote, R., Lane, R., Lim, P., Vitagliano, D., Blier, P., Fava, M., Liebowitz, M., Ravindran, A., Gaillard, R., Ameele, H. V. D., Preskorn, S., Manji, H., Hough, D., Drevets, W. C. & Singh, J. B. (2019). *Int. J. Neuropsychopharmacol.* **22**, 616–630.

Goldberg, J. (1998). *Cell*, **95**, 237–248.

Goto, M., Yamauchi, T., Kamiya, N., Miyahara, I., Yoshimura, T., Mihara, H., Kurihara, T., Hirotsu, K. & Esaki, N. (2009). *J. Biol. Chem.* **284**, 25944–25952.

Hashimoto, K., Fukushima, T., Shimizu, E., Komatsu, N., Watanabe, H., Shinoda, N., Nakazato, M., Kumakiri, C., Okada, S., Hasegawa, H., Imai, K. & Iyo, M. (2003). *Arch. Gen. Psychiatry*, **60**, 572–576.

Hashimoto, K., Fukushima, T., Shimizu, E., Okada, S., Komatsu, N., Okamura, N., Koike, K., Koizumi, H., Kumakiri, C., Imai, K. & Iyo, M. (2004). *Prog. Neuropsychopharmacol. Biol. Psychiatry*, **28**, 385–388.

Howes, O., McCutcheon, R. & Stone, J. (2015). *J. Psychopharmacol.* **29**, 97–115.

Hutchinson, E. G. & Thornton, J. M. (1990). *Proteins*, **8**, 203–212.

Jansonius, J. N. (1998). *Curr. Opin. Struct. Biol.* **8**, 759–769.

Jirásková-Vaníčková, J., Ettrich, R., Vorlová, B., Hoffman, H. E., Lepšík, M., Jansa, P. & Konvalinka, J. (2011). *Curr. Drug Targets*, **12**, 1037–1055.

Kleckner, N. W. & Dingledine, R. (1988). *Science*, **241**, 835–837.

Kleywegt, G. J. & Jones, T. A. (1996). *Structure*, **4**, 1395–1400.

Kumar, K. S. D., Gurusaran, M., Satheesh, S. N., Radha, P., Pavithra, S., Thulaa Tharshan, K. P. S., Helliwell, J. R. & Sekar, K. (2015). *J. Appl. Cryst.* **48**, 939–942.

Labrie, V., Wong, A. H. C. & Roder, J. C. (2012). *Neuropharmacology*, **62**, 1484–1503.

Laskowski, R. A., Jabłońska, J., Pravda, L., Vařeková, R. S. & Thornton, J. M. (2018). *Protein Sci.* **27**, 129–134.

Madeira, C., Lourenco, M. V., Vargas-Lopes, C., Suemoto, C. K., Brandão, C. O., Reis, T., Leite, R. E., Laks, J., Jacob-Filho, W., Pasqualucci, C. A., Grinberg, L. T., Ferreira, S. T. & Panizzutti, R. (2015). *Transl. Psychiatr.* **5**, e561.

Malkesman, O., Austin, D. R., Tragon, T., Wang, G., Rompala, G., Hamidi, A. B., Cui, Z., Young, W. S., Nakazawa, K., Zarate, C. A., Manji, H. K. & Chen, G. (2012). *Int. J. Neuropsychopharmacol.* **15**, 1135–1148.

Mori, H., Wada, R., Li, J., Ishimoto, T., Mizuguchi, M., Obita, T., Gouda, H., Hirono, S. & Toyooka, N. (2014). *Bioorg. Med. Chem. Lett.* **24**, 3732–3735.

Mori, H., Wada, R., Takahara, S., Horino, Y., Izumi, H., Ishimoto, T., Yoshida, T., Mizuguchi, M., Obita, T., Gouda, H., Hirono, S. & Toyooka, N. (2017). *Bioorg. Med. Chem.* **25**, 3736–3745.

Murshudov, G. N., Skubák, P., Lebedev, A. A., Pannu, N. S., Steiner, R. A., Nicholls, R. A., Winn, M. D., Long, F. & Vagin, A. A. (2011). *Acta Cryst.* D**67**, 355–367.

Niciu, M. J., Ionescu, D. F., Richards, E. M. & Zarate, C. A. (2014). *J. Neural Transm.* **121**, 907–924.

Niesters, M., Martini, C. & Dahan, A. (2014). *Br. J. Clin. Pharmacol.* **77**, 357–367.

Otte, D. M., Barcena de Arellano, M. L., Bilkei-Gorzo, A., Albayram, O., Imbeault, S., Jeung, H., Alferink, J. & Zimmer, A. (2013). *PLoS One*, **8**, e67131.

Papouin, T., Ladépêche, L., Ruel, J., Sacchi, S., Labasque, M., Hanini, M., Groc, L., Pollegioni, L., Mothet, J.-P. & Oliet, S. H. R. (2012). *Cell*, **150**, 633–646.

Paul, P. & de Belleroche, J. (2014). *Front. Synaptic Neurosci.* **6**, 10.

Petrenko, A. B., Yamakura, T., Baba, H. & Shimoji, K. (2003). *Anesth. Analg.* **97**, 1108–1116.

Pomarol-Clotet, E., Honey, G. D., Murray, G. K., Corlett, P. R., Absalom, A. R., Lee, M., McKenna, P. J., Bullmore, E. T. & Fletcher, P. C. (2006). *Br. J. Psychiatry*, **189**, 173–179.

Schatzberg, A. F. (2019). *Am. J. Psychiatry*, **176**, 422–424.

Smith, M. A., Mack, V., Ebneth, A., Moraes, I., Felicetti, B., Wood, M., Schonfeld, D., Mather, O., Cesura, A. & Barker, J. (2010). *J. Biol. Chem.* **285**, 12873–12881.

Sun, L., Bartlam, M., Liu, Y., Pang, H. & Rao, Z. (2005). *Protein Sci.* **14**, 791–798.

Swainson, J., Thomas, R. K., Archer, S., Chrenek, C., Baker, G., Dursun, S., MacKay, M. A., Klassen, L. J., Chokka, P. & Demas, M. L. (2019). *Expert Rev. Neurother.* **19**, 899–911.

Takahara, S., Nakagawa, K., Uchiyama, T., Yoshida, T., Matsumoto, K., Kawasumi, Y., Mizuguchi, M., Obita, T., Watanabe, Y., Hayakawa, D., Gouda, H., Mori, H. & Toyooka, N. (2018). *Bioorg. Med. Chem. Lett.* **28**, 441–445.

Traynelis, S. F., Wollmuth, L. P., McBain, C. J., Menniti, F. S., Vance, K. M., Ogden, K. K., Hansen, K. B., Yuan, H., Myers, S. J. & Dingledine, R. (2010). *Pharmacol. Rev.* **62**, 405–496.

Tsai, G., Yang, P., Chung, L.-C., Lange, N. & Coyle, J. T. (1998). *Biol. Psychiatry*, **44**, 1081–1089.

Vasilescu, A. N., Schweinfurth, N., Borgwardt, S., Gass, P., Lang, U. E., Inta, D. & Eckart, S. (2017). *Neuropsychiatr. Dis. Treat.* **13**, 973–980.

Vorlová, B., Nachtigallová, D., Jirásková-Vaníčková, J., Ajani, H., Jansa, P., Řezáč, J., Fanfrlík, J., Otyepka, M., Hobza, P., Konvalinka, J. & Lepšík, M. (2015). *Eur. J. Med. Chem.* **89**, 189–197.

Watanabe, A., Sasaki, T., Yukami, T., Kanki, H., Sakaguchi, M., Takemori, H., Kitagawa, K. & Mochizuki, H. (2016). *Neuroscience*, **339**, 139–149.

Winn, M. D., Ballard, C. C., Cowtan, K. D., Dodson, E. J., Emsley, P., Evans, P. R., Keegan, R. M., Krissinel, E. B., Leslie, A. G. W., McCoy, A., McNicholas, S. J., Murshudov, G. N., Pannu, N. S., Potterton, E. A., Powell, H. R., Read, R. J., Vagin, A. & Wilson, K. S. (2011). *Acta Cryst.* D**67**, 235–242.

Wolosker, H., Sheth, K. N., Takahashi, M., Mothet, J.-P., Brady, R. O., Ferris, C. D. & Snyder, S. H. (1999). *Proc. Natl Acad. Sci. USA*, **96**, 721–725.

Wu, S.-Z., Bodles, A. M., Porter, M. M., Griffin, W. S. T., Basile, A. S. & Barger, S. W. (2004). *J. Neuroinflamm.* **1**, 2.

Yamada, T., Komoto, J., Takata, Y., Ogawa, H., Pitot, H. C. & Takusagawa, F. (2003). *Biochemistry*, **42**, 12854–12865.

Yoshimura, T. (2008). *Seikagaku*, **80**, 324–330.

Zádori, D., Veres, G., Szalárdy, L., Klivényi, P., Toldi, J. & Vécsei, L. (2014). *J. Alzheimers Dis.* **42**, S177–S187.

Zhou, H.-Y., Chen, S.-R. & Pan, H.-L. (2011). *Exp. Rev. Clin. Pharmacol.* **4**, 379–388.